LANGMUIR

pubs.acs.org/Langmuir Article

Retention Forces for Drops on Microstructured Superhydrophobic Surfaces

Shaur Humayun, R. Daniel Maynes, Julie Crockett, and Brian D. Iverson*

Cite This: *Langmuir* 2022, 38, 15960−15972 Read Online

ACCESS | Metrics & More | Article Recommendations | Supporting Information

ABSTRACT: Accurate models of retention forces between drops and superhydrophobic (SH) surfaces are required to predict drop dynamics on the surface. This retention force is, in turn, useful in modeling heat transfer rates for dropwise condensation on a SH surface. Drop contact angle distribution and base area on SH surfaces are essential factors for predicting retention forces. The present work measures the contact angle distribution and base area shapes of various drop sizes over a wide range of solid fraction for inclined microstructured SH surfaces at the point of drop departure. Base area shape was found to be well approximated using two ellipses with different aspect ratios, and the contact angle distribution was found to be best fit by a sigmoid function. At an incline near the roll-off angle, drop base area for surfaces with solid fraction close to 1 and close to 0 were found to be nearly circular, whereas the base area of drops on surfaces with an intermediate solid fraction deviated from circular behavior. In this work, maximum advancing and minimum receding contact angles were found as a function of solid fraction and used to calculate retention forces. Contact angle distribution and base area shapes are then used to calculate retention forces between drops and SH surfaces. These calculations are compared with the component of measured drop weight acting parallel to the plane on a tilted surface for validation. Previous retention force studies that investigate base area shape and contact angle distribution for smooth surfaces are not applicable for microstructured SH surfaces. The work shows that using a sigmoid contact angle distribution and modified base area shape yields retention forces that are on average 50% better than previously reported methods. Retention forces for smooth and SH surfaces calculated in this study were used to suggest retention force factor values for varying solid fraction surfaces.

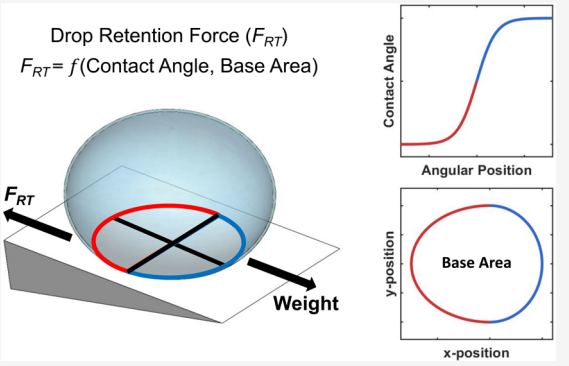

INTRODUCTION

Superhydrophobic (SH) surfaces have gained attention due to their self-cleaning nature, drag-reducing behavior, and alteration in condensation dynamics.[1−3] Applications include oil/water separation, antibacterial and anticorrosion products, electronic hot spot cooling, and improved efficiency condensers, among others.[4−7] An important application of SH surfaces is in promoting dropwise condensation (DWC) which has been shown to increase heat transfer rates by more than 5 times when compared to filmwise condensation.[8] Improvement in condensation heat transfer rate stands to benefit many commercial applications including power generation, refrigeration cycles, desalination, energy conversion, water harvesting, etc.[9] In addition to DWC, heat transfer rates during the condensation process may be further improved by enhancing condensate removal through an external force such as vapor shear or gravity. To remove a drop from a surface, these external forces must overcome the force of retention of the drop to the surface, which is dependent on the drop size, shape, and surface energy. Therefore, it is essential to understand the change in drop retention force as a function of drop shape, size, and varying surface conditions to determine the phase change heat transfer coefficients and condensate removal rates. This work studies the factors, including contact angle distribution and base area shape, that affect the retention force between a drop and a SH surface.

Small drops resting on a symmetrically patterned SH surface in ambient conditions may be spherical in shape. However, the influence of an external force on a drop can result in a nonuniform contact angle distribution around the circumference of drop base and distortion in the base area. Because the contact angle distribution and base area shape/size affect retention between the drop and the surface, if the SH surface roughness is not radially symmetric, local surface energy variations may cause a noncircular drop base area.

For gravity driven drop motion, consider a drop resting on a tilted surface as shown in Figure 1a, which illustrates the contact angle variation and base area distortion. Once the drop

Received: August 23, 2022
Revised: November 23, 2022
Published: December 14, 2022

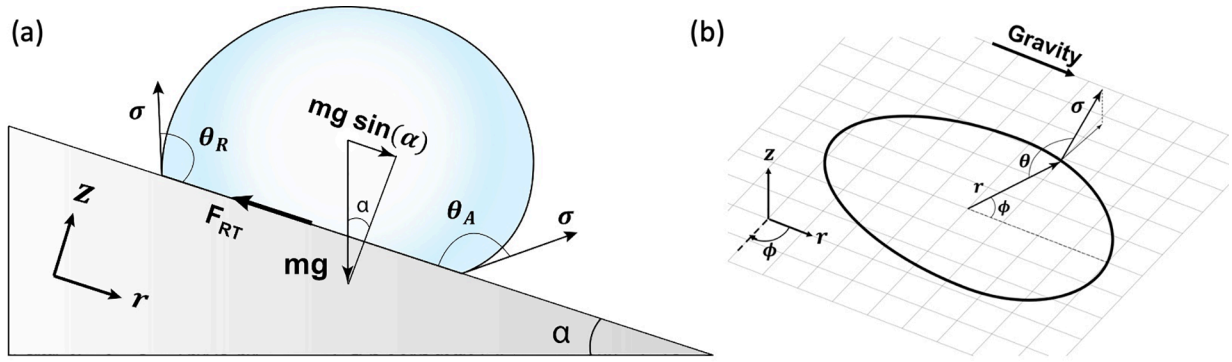

Figure 1. (a) Schematic of a drop on a tilted, hydrophobic surface indicating forces applied to the drop. (b) View of contact line at drop base area where σ is the surface tension, θ is the local contact angle, θ_R is the receding contact angle, θ_A is the advancing contact angle, r is the local radius, ϕ is the azimuthal position in tilted plane, α is the tilt angle, and mg is the drop weight.

has formed, the major forces acting on the drop include the retention force between the drop and surface and the weight component of the force parallel to the surface which can result in the drop moving down the inclined surface (as shown in Figure 1a). For a similar drop on a horizontal surface in shear flow, the drop may also be acted upon by a drag force exerted by the flowing vapor past the drop. An understanding of the forces required to overcome retention and to allow the drop to move can be obtained by a force balance on the drop. These forces are affected by the size and shape of the drop as they affect the retention force, as noted above.

The differential retention force acting along the base of the drop as shown in Figure 1b is given as follows:[10]

$$dF_{RT} = \sigma \cos\theta \cos\phi \, r d\phi \tag{1}$$

The total retention force can then be calculated by integrating eq 1 over the entire base contact line, resulting in eq 2.

$$F_{RT} = 2\sigma \int_0^{\pi} \cos\theta \cos\phi \, r d\phi \tag{2}$$

For a static drop in the absence of vapor flow, the retention force is balanced by gravitational force as

$$F_{RT} = mg \sin\alpha \tag{3}$$

The retention force expression in eq 2 simplifies for a spherical drop; however, the drop base does not always exhibit a circular shape. As a result, the retention force will differ from that observed by ElSherbini and Jacobi,[11] who proposed a predictive retention force model based on a circular base area. Most prior researchers have used a simplified model for retention force that has assumed a spherical drop with a circular base area.[12−20]

In an early work by Furmidge, the work required to move a drop along a surface was modeled with a force balance on a drop.[21] The drop was assumed to have a rectangular base area as it was swept across the surface. For hydrophilic surfaces, Furmidge determined that negative work was done at the receding end and positive work was done at the advancing end of the translating drop. Furmidge's work divided a drop into two portions: one advancing portion with a constant maximum contact angle and one receding portion with a minimum constant contact angle. Korte and Jacobi modified Furmidge's model by assuming a circular drop base area to improve the approximation of drop shape and base area.[22] They used the radius of the drop at the base for hydrophilic surfaces to obtain improved retention force results. Korte and Jacobi also assumed that the contact angle varied linearly from the advancing to receding end. This was in contrast to Extrand and Kumagai,[23] who proposed a cosine variation ($y = m \cos x + c$) from the advancing to receding end of the drop, as compared to Furmidge's original model. In subsequent work, ElSherbini and Jacobi suggested a third-order polynomial function to model contact angle variation with azimuthal angle at the three-phase contact line (TPCL).[11] They observed this third-order variation in contact angle for both smooth hydrophobic and hydrophilic surfaces. They then used this functional form to determine the retentive force factor to simplify the integration of eq 2. Their work showed better agreement than other approaches in predicting the retention force of a spherical drop on an inclined surface. Measurement of the contact angle variation has been performed in the past for smooth hydrophobic surfaces;[24] however, detailed measurements do not exist in the literature for microstructured SH surfaces. Therefore, it is unclear if existing models of the circumferentially varying contact angle apply for microstructured SH surfaces. Addressing this deficiency is one of the objectives of this work.

In addition to contact angle variation, prior works have also explored the base area of drops on varying surface types (hydrophilic and hydrophobic) and of varying roughness. Rotenberg et al. observed drop elongation in the base area along the direction of gravity, or incline, for smooth surfaces ranging from hydrophilic to slightly hydrophobic (siliconed glass slides).[25] Their study sought to minimize the surface free energy using finite element analysis to determine the elongation of a drop and compare it with experimental results. They imaged the drop from side and underneath to observe contact angles and base area shape of a 50 μL drop. Their numerical solution for drop base area shape was consistent with their experimental results; however, they did not consider variation in the contact angle along TPCL. Extrand and Kumagai also studied elongation and back-to-front drop asymmetry, with greater asymmetry observed on surfaces with large contact angle hysteresis.[23] They also observed a linear relation between the drop aspect ratio and contact angle hysteresis for smooth hydrophilic surfaces. Dussan and Chow assumed the front and back of the drop base area were composed of circular arcs connected with parallel sides (i.e., pill-shaped) and elongated in the direction of surface incline.[26] Their model was shown to apply for conditions of small contact angle hysteresis.

https://doi.org/10.1021/acs.langmuir.2c02290
Langmuir 2022, 38, 15960−15972

Sommers and Jacobi explored both contact angle and base area shape variation simultaneously on an aluminum surface with microgrooves aligned with the direction of incline.[27] Their results suggested that the third-order fit for contact angle distribution along azimuthal position used by ElSherbini and Jacobi[11] was a poor representation for variation on grooved surfaces. They also observed that the maximum contact angle was positioned at an azimuthal angle of 90° rather than at the advancing end. They suggested that it was due to the pinning effect of the drop over the groove wall at the 90° azimuthal angle.

ElSherbini and Jacobi[24] were the first to suggest an elliptical model for the base area composed of two ellipses of different aspect ratio, although Extrand and Kumagai's data indicated a distorted ellipse as the base area for drops on hydrophilic surfaces.[23] ElSherbini and Jacobi observed that using a single ellipse with equivalent base area to dual ellipse base resulted in similar retention force results. They proposed a curve fit that predicts the aspect ratio of a drop base as a function of Bond number, and this was observed to fit the data from Extrand and Kumagai well.

Few prior studies have observed contact angle variation with azimuthal position. Antonini et al. introduced image based adhesion force analysis to measure the circumferentially varying contact angle for a hydrophobic surface.[28] In addition, Antonini et al. used a numerically discretized technique to calculate the total retention force from experimentally measured contact angle and base area. Although contact angle variations have been observed in prior works on smooth inclined surfaces, the measurement of corresponding base area shape of drops has not been characterized in prior literature.

In addition to drop shape, surface texture also has a significant effect on the retention force of a drop. When condensate forms as water vapor flows past a cooled surface, the drop dynamics depend on the surface roughness and the characteristics of the flow. It has been shown that, for a microstructured SH surface,[29] condensate forms in cavities comprised of valleys between asperities and grows in a Wenzel state. The drop remains in a Wenzel state until it reaches a critical volume and contact angle threshold, and then the drop transitions to the Cassie−Baxter state.[30] For a SH surface with both micro- and nanoscale texture, drops tend to have a smaller transition threshold resulting in transition to the Cassie−Baxter state at smaller volumes.[31] To explore the effects of cavity characteristics, Masashi et al. studied sliding angles (the angle at which a drop begins translating along an inclined plane) for drops on SH surfaces with various roughness.[32] The surfaces had an average roughness of 59 nm and an average contact angle between 105° and 160°. The ratio of total area to projected area (inverse of solid fraction) was about 1.8 on average. The degree of hydrophobicity was varied by changing the coating material to alter the static contact angle. They observed that the sliding angle generally decreased with increasing contact angles. Surfaces with circular post structures were observed to have different contact angles and wetting properties than surfaces with ribbed or grooved structures.

Prior to this work, some researchers have used a retentive force factor (k) to characterize the retention forces for drops on various surfaces.[11,33] This k factor depends on the predicted or measured values for drop shape and contact angle distribution, resulting in a range of reported values. The most commonly used approach for determining k is that reported by ElSherbini and Jacobi.[11] They calculated k by solving the closed form of the retention force integral equation assuming a circular base shape and using their proposed third-order polynomial contact angle distribution function. However, Kim et al. showed that the value of factor k proposed by ElSherbini and Jacobi was not a good fit for water drops on smooth hydrophobic surfaces and suggested a higher value of the factor k than the value proposed by ElSherbini and Jacobi.[33]

This work extends a similar retention force analysis originally presented by ElSherbini and Jacobi for smooth hydrophobic and hydrophilic surfaces to microstructured SH surfaces.[11] We experimentally characterize the contact angle distribution and base area of water drops on tilted, micropillar-structured SH surfaces to determine the retention force between a drop and the surface. The circumferential contact angle distribution for drops of different volumes are experimentally determined on microstructured SH surfaces for varying surface solid fraction and compared with existing distributions. The measured base area shape of the drop is also compared with prior models. The experimental measurements are shown to provide a better understanding of base area elongation and drop deformation for microstructured SH surfaces, resulting in an improved calculation of drop retention forces. We also present our results for the retention factor k for smooth surfaces as determined from experimentally obtained retention forces and compare it to values found in the literature under similar conditions. In addition, we report values of k for microstructured SH surfaces for the first time.

The remainder of this paper is structured as follows. First, the experimental procedures for surface preparation and data acquisition of drop images are described. Next, results of contact angle and base area measurements are presented as a function of surface solid fraction, and the process of computing retention force between the drops and the surface is presented in detail. The predictions of retention force are compared to measured values, and conclusions of the study are summarized.

METHODS

Surface Fabrication. Smooth hydrophobic surfaces were created using silicon wafers of 100 mm diameter. Polished stock wafers were cleaned with acetone and isopropyl alcohol and dried for 15 min at 150 °C. After cleaning, a 100 nm layer of chromium was deposited on the surface using a Denton Vacuum E-Beam evaporator. Cr coating was chosen because of its wear resistance and durable adhesion to Si as well as Teflon.[34] Teflon-AF 1600 was then spin-coated on the surface at 1000 rpm for 20 s using a 0.6% solution (by weight in FC-40). Coated wafers were heated gradually to 330 °C on a hot plate to dry the fluoropolymer film on the surface. A second coat of Teflon was then added in the same manner after dicing the wafers into smaller samples for experiments. This results in a uniform coating of 0.6% Teflon solution of approximately 50 nm in thickness.

SH surfaces were also created using silicon wafers where after the cleaning process wafers were patterned using photolithography and etched to create a rectangular array of circular micropillars (see the Supporting Information). Wafers were spin-coated with a negative photoresist, and the photoresist was exposed to light in an MA150 Karl Suss Aligner. The wafers were heated again and then developed in AZ300 MIF developer. With the photoresist now patterned, wafers were etched using an STS ICP etcher with an inductively coupled plasma process to a depth of about 15 μm. The photoresist was removed in Nanostrip at 90 °C for 2 h. Any residual photoresist was removed using an oxygen plasma etch. Microstructured wafers were coated with 100 nm of chromium in a vacuum E-Beam evaporator. Two coats of Teflon-AF 1600 were then applied to the micro-

https://doi.org/10.1021/acs.langmuir.2c02290
Langmuir 2022, 38, 15960−15972

Table 1. Geometric Characteristics for Surfaces Used in This Study[a]

solid fraction	pitch (μm)	pillar diameter (μm)	pillar height (μm)	static CA (deg)	drop volume (μL)	receding CA (deg)	advancing CA (deg)	x_S (deg)	average x_S (deg)
1.00	n/a	n/a	n/a	115	20	109	119	79	81
					30	109	119	80	
					40	109	117	84	
0.40	24.0	17.1	15.0	145	20	123	146	72	70
					30	125	147	69	
					40	122	144	68	
0.26	12.0	6.9	11.0	150	10	134	156	68	70
					20	133	154	71	
					30	135	156	71	
					40	135	152	72	
0.09	16.0	5.5	12.2	158	10	146	162	83	80
					20	147	161	79	
					30	146	161	79	
0.03	16.0	3.1	12.0	160	10	148	163	78	79
					20	149	161	81	
					30	148	162	78	

[a]Static contact angles have an uncertainty of ±1°.

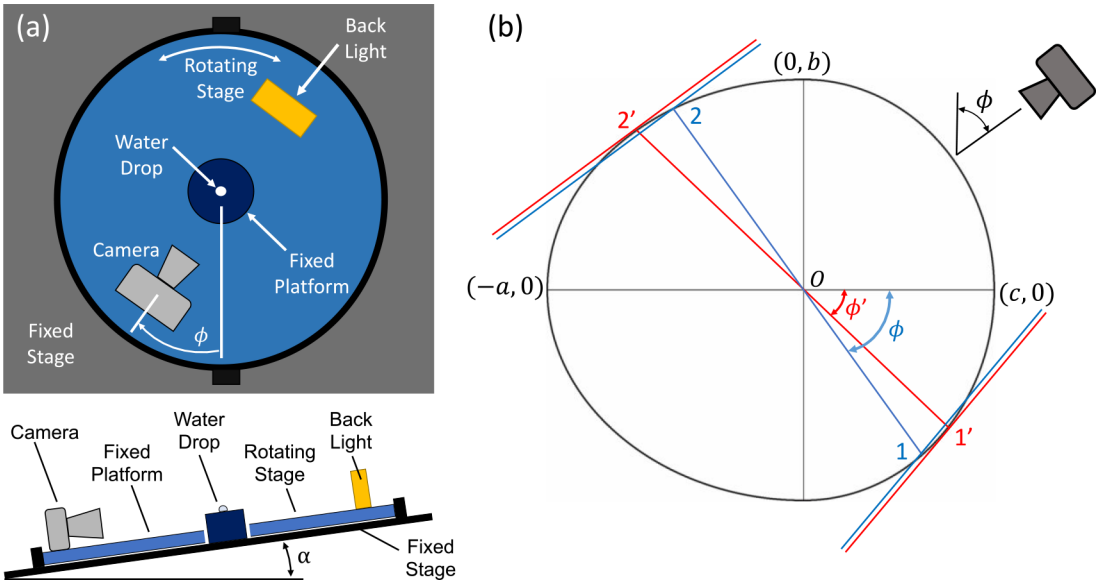

Figure 2. (a) Experimental setup used for contact angle and base area measurements. (b) Drop base area contour showing the difference in recorded azimuthal position and actual azimuthal position for a noncircular base area. The camera has been moved by ϕ relative to the center line; however, the values are being recorded at ϕ'.

structured surface using the same process as outlined above for smooth surfaces.

Five surfaces of varying solid fraction (ratio of pillar projected area to total planform area) were used in this study (F_S = 1, 0.4, 0.26, 0.09, and 0.03). The microstructure consisted of a rectangular array of circular pillars with varying diameter and pitch with pillar heights between 11 and 15 μm. Pitch is defined as the smallest distance from the center of one pillar to the center of neighboring pillar, when viewed from top. Details of surface features are reported in Table 1. A wide range in solid fraction was tested as a part of this study to examine its influence on base area and contact angle distribution for drops on SH surfaces.

Contact Angle and Base Area Measurements. Measurements for circumferentially varying contact angle and base area were performed using a rotating stage and DSLR camera as shown schematically in Figure 2a. Because a drop resting on a SH surface has a larger projected drop area than base area, the drop cannot be imaged from the top to obtain base area shape or contact angles. Therefore, the drop was imaged from the side using a rotating stage. Each hydrophobic or SH surface was rigidly fixed at the center of the rotating stage while the camera and backlight were rotated around the test surfaces. Deionized water drops of 10−40 μL were placed on the surface using a micropipet (uncertainty ±0.1 μL). The entire rotating stage was tilted to an angle just below the drop roll-off angle, and the camera was rotated around the static drop to capture 36 images in 5° increments. The images were then processed using a MATLAB computer vision code to obtain the contact angle and base area geometry of the drop. For each scenario considered, measurements were averaged over six or more realizations.

Binary forms of the images were used to obtain the drop contours in each image. A fifth-order polynomial function was fit to the edges of the drop in each image, and the gradient of the function fit at the drop edges was used to compute the drop contact angles at each position ϕ. From the measured contact angle distribution, advancing and receding values are extracted and summarized in Table 1.

An approach similar to contact angle measurement was taken to obtain base area measurements. Binary forms of the images were used to obtain the drop contour, and a second-order polynomial function

https://doi.org/10.1021/acs.langmuir.2c02290
Langmuir 2022, 38, 15960−15972

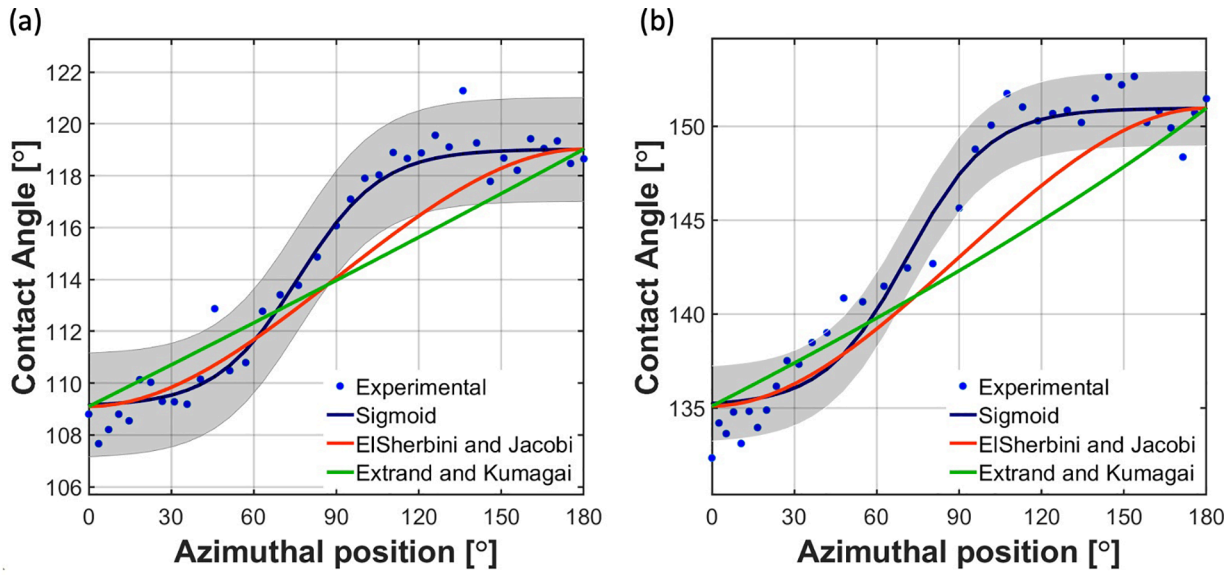

Figure 3. Measured contact angle distribution compared to the predicted behavior by ElSherbini and Jacobi[11] as well as Extrand and Kumagai[23] for a 40 μL drop on (a) a smooth hydrophobic surface ($F_S = 1$) and (b) a microstructured SH surface ($F_S = 0.26$) with the gray region representing the uncertainty in contact angle ($\pm 2°$).

was fit to the top of the drop contour to determine the highest point of the drop. The highest point of the drop was recorded in each image and was then used as a reference to measure the drop height and base diameter.

As explained in ref 24, there is a perspective error associated with noncircular drop contact line coordinates. The perspective error can be understood with the help of Figure 2b. To determine the actual base area geometry of a noncircular area, the recorded position for contact angle and base area measurements were corrected using the aspect ratio of receding and advancing ellipses. From Figure 2b, the advancing aspect ratio is calculated as c/b and receding aspect ratio is calculated as a/b, both defined with a common denominator. When the camera is rotated to an angle ϕ on the rotating stage, it views point 1′ and 2′ of the drop contour. If the drop contour were circular, the camera would have seen points 1 and 2. To calculate the corrected angular position (ϕ'), the drop contour is taken to be a combination of two ellipses. When the camera is parallel to the vertical and horizontal axes of drop in Figure 2b, no distortion exists when viewing the drop base. Hence, the lengths a, b, and c can be measured without angle correction which can be used to calculate axes ratios. After some algebraic manipulation, the following relation can be used to calculate the corrected angle position (detailed calculations can be found in ref 24):

$$\tan \phi' = \frac{\tan \phi}{\beta^2} \tag{4}$$

where β_2 is the advancing aspect ratio (b/c) for angles between 0°−90° and 270°−360° and β_1 is the receding aspect ratio (a/b) for angles between 90°−270°. Typical values for angle correction are on the order of 0°−3°, with larger drops having larger angle corrections.

Once the images are acquired and analyzed, results are used to recreate the drop's contact line to obtain the base area, and contact angles are plotted against corrected coordinates to obtain the contact angle distribution. Values or relationships for the contact angle distribution and ellipses can then be substituted in eq 2 for calculating the retention force.

Because the time required to image each drop was large, drops were observed to evaporate appreciably during the period of imaging. To eliminate evaporation effects, experiments were performed in a room where the relative humidity (RH) was maintained between 65% and 75%. The surface tension (σ) of deionized water was measured for each experiment to eliminate variations due to any variations in RH and temperature. Capillary tubes (borosilicate glass from Pyrex) with a diameter (D) of 1.2 mm were immersed in deionized water, and the rise in height of the liquid was measured with eq 5 to determine the surface tension[35]

$$\sigma = \frac{\rho g D h}{4 \cos \theta_G} \tag{5}$$

where ρ is the water density and θ_G for the water−glass contact was approximately zero.

Experiments were performed on four different samples of each surface solid fraction, and the results were averaged over six or more realizations (two realizations for each surface). Five different solid fractions were used for this study (solid fraction of 1, 0.4, 0.26, 0.09, and 0.03) for the micropillar surfaces (Table 1). In addition, experiments were performed at multiple different positions on the same surface to avoid the influence of random surface variations. An azimuthal position correction was performed for each measurement before averaging the results (Figure 2b).[24]

Uncertainty Analysis. All contact angle measurements were obtained using the image analysis described above, and the uncertainty in the measured contact angle is based on a 95% confidence interval. This was determined by calculating the standard deviation of the data over at least six independent measurements. The uncertainty in the drop base length (contact line between the drop and the surface as viewed from the side and used to determine contact area shape) was calculated by considering the contribution of image resolution used for calibration (conversion from pixels to mm) and the standard deviation from the six realizations. The uncertainty in surface tension was also calculated by propagating the uncertainty in all parameters used in eq 5. Because the parameter space for retention force is six-dimensional (σ, θ_A, θ_R, ϕ, a, β), Monte Carlo simulations with Latin hypercube sampling were used to calculate the total uncertainty. Random parameter values were selected between their extremes and then used to calculate the quantity of interest. The standard deviation in the quantity of interest was reported as uncertainty. Latin hypercube sampling divides the parameter space into smaller, evenly distributed parameter spaces for efficient random sampling over their domains.

RESULTS AND DISCUSSION

Experiments were performed for drop volumes ranging from approximately 10 to 40 μL. The range of drop volumes was chosen based on the minimum and maximum roll-off angles

https://doi.org/10.1021/acs.langmuir.2c02290
Langmuir 2022, 38, 15960−15972

that could be accommodated with the current setup. Any drop volume less than approximately 10 μL has a roll-off angle >15°, and the setup becomes very sensitive to nearby movements and vibrations at these high angles. As a result, unreliable data at 10 μL have been omitted. Because the camera is moved around the drop manually, any induced vibration causes the drop to start oscillating and potentially slide down the surface, as droplets are quite mobile on superhydrophobic surfaces. The time duration to take data on one drop is approximately 10 min. For drop sizes higher than 40 μL, the surface area of the drop becomes large enough that evaporation effects become appreciable. In addition, large drops also become very sensitive to vibrations induced to the setup also causing roll-off at very small angles.

Contact Angle Distribution. The contact angle distribution around the entire circumference of the drop base was obtained for each drop volume explored. These measurements were obtained at a surface tilt angle that was slightly lower than the roll-off angle. For all cases the surface inclination angle is within 0.5° of the angle at which drop started to roll. Figure 3a shows averaged results for a 40 μL drop on smooth hydrophobic surfaces (F_s = 1). The measured results represent data at each ϕ averaged from four unique smooth surfaces. The advancing contact angle, θ_A, exists at an azimuthal location of ϕ = 180°, and the receding angle, θ_R, exists at ϕ = 0°. The red line in the figure represents the third-order polynomial distribution for contact angle that has been suggested by ElSherbini and Jacobi for smooth hydrophobic surfaces.[11] The green line represents the cosine distribution for contact angle suggested by Extrand and Kumagai also for smooth hydrophobic surfaces.[23] The gray region represents the uncertainty in contact angle measurements calculated to be ±2°, as described above in the section addressing uncertainty. Although the functions suggested by ElSherbini and Jacobi as well as Extrand and Kumagai lie nearly completely within the gray uncertainty band for smooth hydrophobic surfaces (Figure 3a), the curvature of the data does not follow the suggested function.

Results are shown in Figure 3b for a 40 μL drop on microstructured SH surface with a solid fraction of F_S = 0.26. The difference between advancing and receding contact angles is much more significant (17°) for this surface than for the smooth surface (10°). The F_S = 0.26 surface was chosen as it showed the greatest elongation in drop shape and hence represents the most extreme scenario of all surfaces considered. Note the differences on vertical axis range in Figures 3a and 3b. For the micropillar structured SH surface, the previously reported third-order polynomial and cosine distributions diverge significantly when compared to the measured contact angles.

As revealed by the data of Figures 3a and 3b, the curvature of the contact angle distribution differs notably from that for previously reported works. For the smooth hydrophobic surface, the contact angle remains nearly constant from 0 ≤ ϕ ≤ 20°, then it changes rapidly from 20° ≤ ϕ ≤ 100°, and then it levels off to nearly a constant value between 100° ≤ ϕ ≤ 180°. The variation in θ is even more pronounced for the F_S = 0.26 surface. Here, θ remains nearly constant for the entire advancing portion of the drop (90° ≤ ϕ ≤ 180°). Recall that previously Furmidge[21] proposed a model for retention force calculation that assumed θ was constant at θ_R along the entire receding portion of the drop and at a value of θ_A along the entire advancing side of the drop.

The experimental data of Figure 3 follow the shape of a sigmoid function, and the blue lines represent sigmoid fits to the data. As shown, the sigmoid fit matches the curvature of the data much more closely than the third-order polynomial distribution and the Furmidge's assumption of constant values of θ_A and θ_R along the advancing and receding sides of the drop. The standard form of a sigmoid function that is symmetric about the y-axis is expressed as follows:

$$y = \frac{1}{1 + e^{-x}} \tag{6}$$

Equation 6 is modified to fit the data as follows:

$$\theta(\phi) = \frac{\theta_A - \theta_R}{1 + e^{-(12/180)(\phi - x_s)}} + \theta_R \tag{7}$$

Each constant in the sigmoid function has physical significance and can be related to other physical characteristics. The standard function in eq 6 is within 0.25% of the maximum value of the function at x = 6 and is within 0.25% of the minimum value of the function at x = −6. Thus, 99.5% of the total functional range lies between $-6 \le x \le 6$ and is taken to be the domain of the function. This domain span of 12 units (from −6 to 6) is then scaled to 180 units (from 0 to 180°) for the azimuthal position; hence the coefficient 12/180 in the exponential function of eq 7.

The shift (x_S) in eq 7 was obtained using a gradient-based optimizer (interior-point algorithm using fmincon, MATLAB) by minimizing the mean error between the sigmoid fit and experimental data. For Figures 3a and 3b, the sigmoid function was plotted using x_S at a given drop volume for a given surface solid fraction (averaged over at least six repeat measurements). The x_S values for each drop volume over all surface solid fractions are reported in Table 1. As shown in Table 1, x_S does not vary significantly with drop volume. The shift along the x-axis is within ±2° of the average x_S reported for all surfaces (Table 1). At ϕ = 90° the differential retention force is zero because the TPCL at this point is parallel to the line of force. Therefore, contact angle values at ϕ > 90° (between $(-a, 0)$ and $(0, b)$ in Figure 2b) are expected to have values lower than the static contact angle on the same surface, and at ϕ < 90° (between $(0, b)$ and $(c, 0)$ in Figure 2b) the contact angle is expected to be higher than the static contact angle. The function in eq 6 can be shifted vertically upward by introducing a bias so that the minimum value is θ_R, and the amplitude of the function represents the maximum contact angle hysteresis ($\theta_A - \theta_R$), yielding a maximum value of θ_A.

The mean and maximum errors between the sigmoid function and the averaged data for the F_S = 0.26 surface (Figure 3b) are 0.2° and 2.9°, respectively. In contrast, the mean and maximum errors between the third-order polynomial and the average data are 0.4° and 6.2°, respectively. The mean and maximum errors between the cosine distribution and the average data are calculated to be 0.6° and 8.5°, respectively. The sigmoid function also provides better characterization for the smooth HPo, although the improvement here is less significant. The correlation coefficient (R^2) for the third-order polynomial and cosine function with the average smooth surface data is 0.96 and 0.94, respectively, while for the sigmoid R^2 = 0.98. The mean and maximum errors between the smooth surface data and the sigmoid function are 0.1° and 1.7°, respectively. The third-order and cosine functions have mean and maximum errors relative to the smooth surface data of 0.2°

https://doi.org/10.1021/acs.langmuir.2c02290
Langmuir 2022, 38, 15960−15972

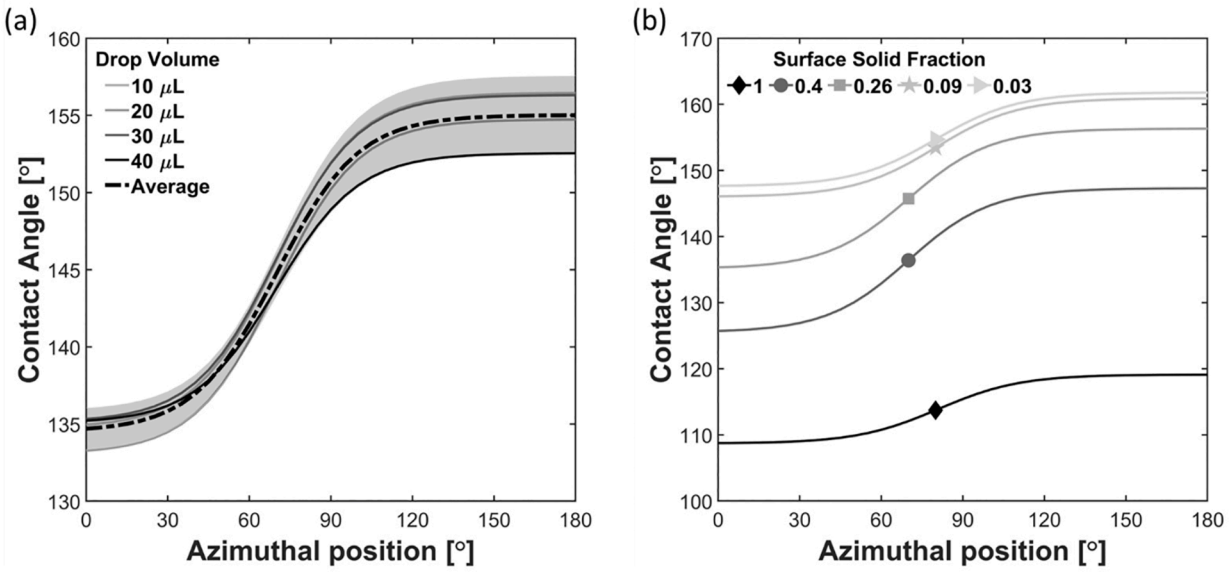

Figure 4. Contact angle distribution at the surface roll-off angle for (a) varying drop volume (10−40 μL) on a F_S = 0.26 solid fraction surface and (b) SH surfaces of varying solid fraction for a 30 μL drop volume.

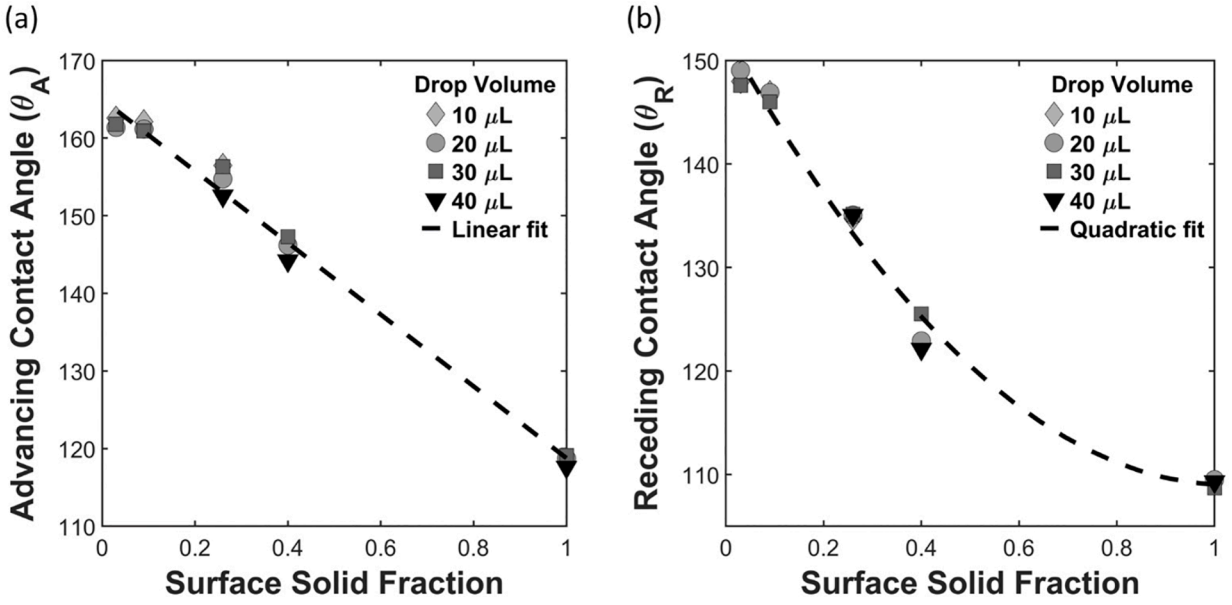

Figure 5. Advancing (a) and receding (b) contact angles as functions of solid fraction for drop volumes of 10, 20, 30, and 40 μL. Linear (a) and quadratic (b) least-squares fits of the data are also shown.

and 3.3° and 0.3° and 3.8°, respectively. In general, it was observed that the third-order polynomial and cosine functions yield better prediction of the contact angle distribution for surfaces with smaller contact angle hysteresis than those with large hysteresis.

Contact angle distributions were experimentally obtained for drop volumes ranging from 10 to 40 μL and solid fractions ranging from 0.03 to 1. Sample sigmoid curve fits are shown in Figure 4. Shown in Figure 4a is the contact angle as a function of ϕ for F_S = 0.26 and all four drop volumes considered. For this plot, the x_S and advancing/receding contact angles used in the sigmoid function are specific to measurements for each drop volume. The dashed line labeled "average" is the sigmoid function obtained when averaging x_S and advancing/receding contact angles over drop volume for F_S = 0.26 (Table 1). An important finding from this work is illustrated by the results shown in Figure 4a (F_S = 0.26). These results clearly show that within the uncertainty band associated with the measurements (gray region Figure 4a) the contact angle distribution and associated x_S are independent of the drop volume for the ranges considered (see the Supporting Information for the data set). This behavior supports the drop growth modes suggested by Liu et al., who showed that drop growth modes are dependent on the least interfacial free energy change rate.[31] The two growth modes are (1) an increase in drop volume with increasing contact angle but at constant drop radius and (2) an increase in volume at constant contact angle but increasing radius. Generally, small drops are observed to grow with increasing contact angle and constant radius until transitioning at critical values of contact angle and drop

https://doi.org/10.1021/acs.langmuir.2c02290
Langmuir 2022, 38, 15960−15972

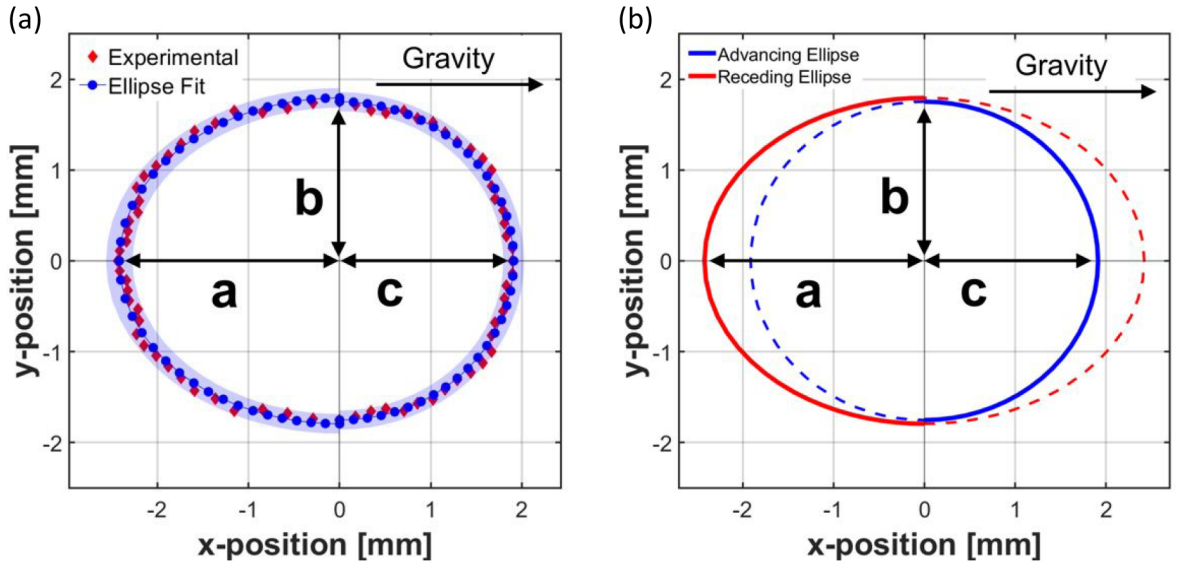

Figure 6. (a) Base area composed of a dual ellipse for a 30 μL drop volume on a F_S = 0.26 SH surface (with gravity acting from left to right, consistent with Figure 1a). The advancing ellipse on the right is observed to be nearly circular with a different axis ratio than the receding ellipse. The light blue band represents the uncertainty. (b) Schematic showing advancing and receding ellipses that comprise the base area of the drop.

volume. Above this critical point the drops then grow with increasing radius and approximately constant contact angle. For all the drop volumes used in this work, the contact angle distribution is independent of volume, suggesting that the minimum drop volume is above the critical volume and in a nonwetting state.

Figure 4b illustrates the contact angle distributions for all five solid fractions at a drop volume of 40 μL. Here, the sigmoid function was obtained by using the average x_S and average advancing/receding contact angles over drop volume (for a given solid fraction). Values of x_S from Table 1 and Figure 4b show that x_S for extreme surface solid fractions (1, 0.09, and 0.03) are close to 80°. For intermediate solid fractions (0.40 and 0.26), the value of x_S is close to 70°. The contact angle data of Figure 4b show that decreasing F_S yields the well-known behavior of increasing contact angle. Recall that all results shown here are at a surface tilt angle that is within 0.5° of the roll-off angle for the surface. It is important to note that the contact angle hysteresis ($\theta_A - \theta_R$) first increases with increasing F_S. This trend is then followed by a decrease in the hysteresis as the solid fraction increases further. This behavior is similar to that observed in the droplet elongation data, which will be discussed later. For the present data, the maximum hysteresis occurred for the F_S = 0.40 surface, which was modestly higher than for the F_S = 0.26 surface.

If the maximum advancing and minimum receding contact angles are known as a function of F_S, then eq 7 can be used to determine the contact angle distribution. Then this distribution can be used with eq 2 to calculate retention forces for drops on inclined surfaces. Thus, it is desirable to know the advancing and receding contact angles for a given solid fraction. Advancing and receding contact angles at an inclination angle just prior to roll-off are shown as a function of solid fraction for SH surfaces in Figure 5 for all drop volumes considered. Both the advancing and receding contact angles decrease with increasing solid fraction, suggesting that all the drops were in a nonwetting state (either Cassie–Baxter or partial wetting state[31]) as discussed earlier. The data of Figure 5 reveals the functional dependence that exists for both the advancing and receding contact angles as a function of solid fraction.

The advancing angle was found to be best predicted by a linear fit with a correlation coefficient value of 0.99, as shown in Figure 5a, and receding angle was found to be best predicted by a second order polynomial fit with a correlation coefficient value of 0.99, as shown in Figure 5b. Equations representing the fits are as follows:

$$\theta_A = 164.99 - 0.4623F_S \tag{8}$$

$$\theta_R = 0.0042F_S^2 - 0.85F_S + 152.36 \tag{9}$$

Equations 8 and 9 allow the contact angle distribution to be known for any surface solid fraction microscale poststyled SH surface, without the need for experimental measurement. Once these values are determined, the entire contact angle distribution can be predicted from eq 7. Unfortunately, droplet elongation is also affected by the SH surface characteristics, and as will be shown below, the dependence is more complicated.

The Cassie–Baxter equation provides a theoretical prediction of static contact angle on microstructured surfaces and is expressed as[36]

$$\cos\theta_{app} = F_S\cos\theta_I + F_S - 1 \tag{10}$$

θ_{app} is the apparent contact angle on the microstructured surface, and θ_I is the intrinsic contact angle on a smooth surface with the same surface chemistry. Equation 10 suggests that as $F_S \to 0$ that the static contact angle approaches 180°. This behavior is not observed in the data of Figure 5. While eqs 8 and 9 predict contact angles that agree with Cassie–Baxter predictions at large and intermediate values of F_S, a notable deviation exists as $F_S \to 0$. The data show that both the advancing and receding contact angles plateau and approach constant values that are notably smaller than 180°. This is likely a result of local pinning of the drop on the microscale features.

https://doi.org/10.1021/acs.langmuir.2c02290
Langmuir 2022, 38, 15960–15972

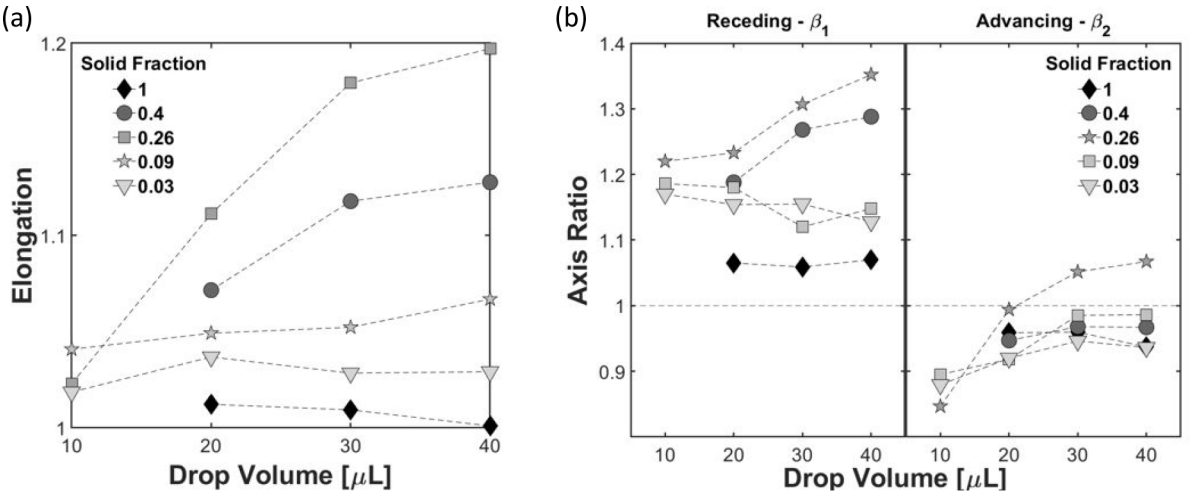

Figure 7. (a) Drop elongation at the roll-off angle for all drop volumes explored as a function of surface solid fraction. (b) Advancing (β_2) and receding (β_1) axis ratios at the roll-off angle for all drop volumes and surface solid fractions considered.

Base Area. A second required parameter to calculate the retention force is the base area shape, which can be defined by the local radial distance from the center of drop as a function of azimuthal position ($r(\phi)$). The base area of each interrogated drop in this work was observed to be well represented by the combination of two ellipses: one on the receding side and one on the advancing side of the drop. This is illustrated in Figure 6a. The light blue region shown in Figure 6a represents the uncertainty in base area measurement, as previously described in the Uncertainty Analysis section. The average error, based on a 95% confidence interval, for the position measurement was ±0.015 mm.

To quantify the extent of drop deformation, a measure of drop elongation is introduced as

$$\text{elongation} = \frac{a + c}{2b} \tag{11}$$

where a, b, and c are the lengths as shown in Figure 6. If the drop is circular at its base, the elongation value will be unity. However, an elongation ratio of unity may not necessarily result in a circular base area, as will be discussed later. Elongation values larger than one are indicative of drop extension along the direction of the gravitational force, and values smaller than one are indicative of elongation perpendicular to the line of gravitational force. Figure 7a shows the elongation as a function of drop volume for varying solid fraction surfaces. Measured elongation values for F_S = 1 indicate that the drop base area is circular and the circular base assumption used by ElSherbini and Jacobi is valid for high solid fractions. However, elongation values appear to initially rise and then fall with decreasing solid fraction. Surfaces with a solid fraction of F_S = 0.03 and 0.09 are also observed to have a circular base area. This is expected due to very low roll-off angles that exist for these surfaces and the assumption of a circular base appears to be valid for very small solid fraction surfaces. Although drops on the F_S = 0.03 and 0.09 surfaces exhibit a circular base area, their contact angle distribution still follows a sigmoid function as opposed to a polynomial relation. Thus, prediction of the retention force should be accomplished with the method described in this work and not that for a circular base.[11] Elongation deviates the most from unity for surfaces with intermediate solid fractions (F_S = 0.4 and 0.26). This is consistent with the high roll-off angles and large contact angle hysteresis that was observed for these surfaces. In addition, at large and small values of the solid fraction (near F_S = 1 and F_S = 0) the elongation is largely independent of drop volume. At intermediate values of F_S (0.26 and 0.4) this is not the case, where for these surfaces the elongation increases dramatically as the drop volume increases.

Axis ratios were plotted for the receding and advancing portions of the contact area base, as shown in Figure 7b. The receding axis ratio is $\beta_1 = a/b$ and the advancing axis ratio is $\beta_2 = c/b$. For the smooth HPo surface (F_S = 1), β_1 and β_2 are both close to unity, with β_1 being slightly greater than 1 and β_2 being slightly smaller than 1. This behavior exists irrespective of drop volume. While the elongation values shown in Figure 7a for the F_S = 0.03 surface are nearly unity (suggesting a circular base area) the values of β_1 and β_2 values deviate notably from unity. In this instance, the receding end of the drop elongates in the direction of gravity, and there is a corresponding reduction of length observed at the advancing end of the drop. This provides an example of how the elongation value can be close to unity but with β_1 being larger than unity and β_2 being less than unity. The β values shown in Figure 7b quantify how much the advancing and receding sides of the drops deviate from being circular.

The results of Figure 7b reveal that the drops elongate more on the receding side of the drop than on the advancing side. This is most pronounced at intermediate values of the solid fraction (F_S = 0.26 and 0.4). In addition, at these intermediate values of solid fraction the elongation on the receding side of the drop increases dramatically with increasing drop volume. On the advancing side of the drop, for the majority of drop volumes and F_S considered, β_2 is consistently in the range 0.95−1.05. The behavior of greater elongation on the receding side of the drop can be understood using the analogy of an elastic material that is adhered to a surface and is being pulled off. Elastic deformation (elongation) occurs on the receding side. However, toward the advancing side, the drop tries to resist gravity by letting the advancing contact angle increase without elongating length c (Figure 6a). This can also explain the larger change in contact angle on the receding side (between $(-a, 0)$ and $(0, b)$ in Figure 2b) as compared to the change observed on advancing side (between $(0, b)$ and $(c, 0)$ in Figure 2b). Because the arc length of a drop base contact line between points $(-a, 0)$ and $(0, b)$ is larger compared to

https://doi.org/10.1021/acs.langmuir.2c02290
Langmuir 2022, 38, 15960−15972

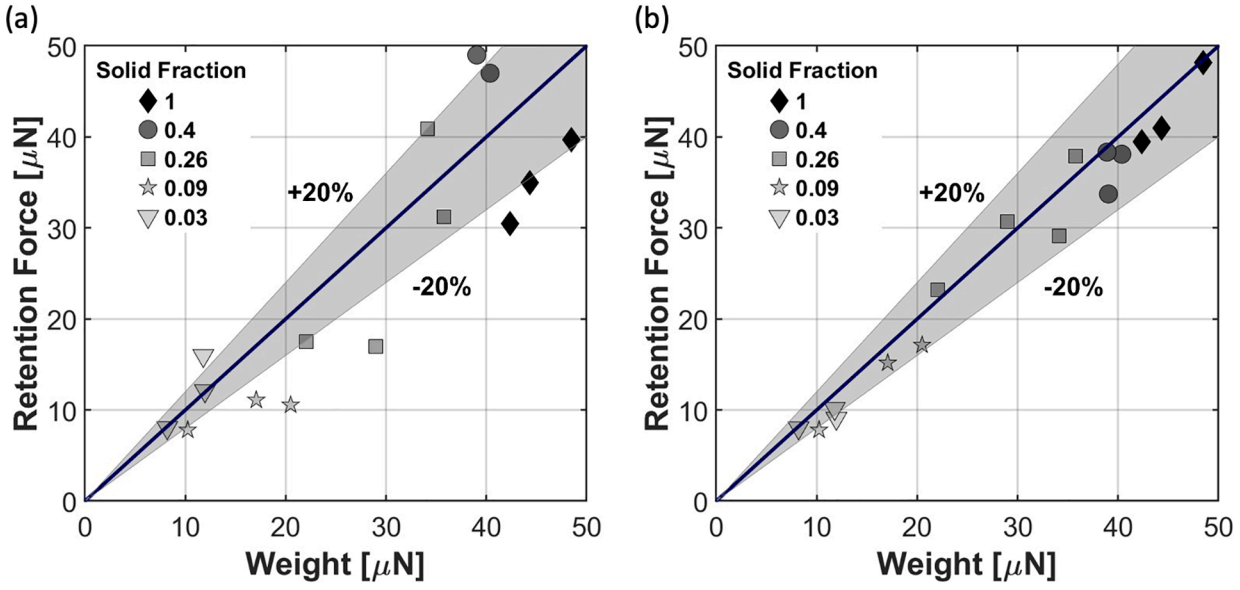

Figure 8. Predicted retention force plotted against measured gravitational force at roll-off for comparison. (a) Retention force was calculated using a circular base assumption and a third-order polynomial contact angle distribution suggested for smooth HPo and microstructured SH surfaces.[24] (b) Retention force was calculated using the sigmoid function introduced in this work and a dual elliptical base area. The gray region represents a ±20% range.

the arc length between points $(0, b)$ and $(c, 0)$ in Figure 2b, the contact angle change is larger to yield maximum retention to the surface. The larger arc length on the receding side also explains the resulting values for x_S. Because the average rate of change in contact angle over the receding side is larger than at the advancing side, the average x_S is caused to be less than 90°. Prior works reporting contact angle distributions assumed symmetry about the 90° azimuthal position. Experimental results and the fitting values for x_S from this study show that the contact angle distribution for drops on microstructured SH surfaces are not symmetric about the 90° azimuthal position.

Retention Forces. Now that both the contact angle distribution and the base area shape are known, this information can be used in the integral force equation (eq 2) to calculate the total retention force acting on the drop. The resulting retention forces are such that the total force can be obtained by summing forces at both ends of a drop, as follows:

$$F_R = 2\sigma \int_0^{\pi/2} \cos\left(\frac{\theta_A - \theta_R}{1 + e^{-(12/180)(\phi - x_S)}} + \theta_R\right) \times \left[\frac{a}{\sqrt{\cos^2\phi + \beta_1^2 \sin^2\phi}}\right] \cos\phi \, d\phi \quad (12)$$

$$F_A = 2\sigma \int_{\pi/2}^{\pi} \cos\left(\frac{\theta_A - \theta_R}{1 + e^{-(12/180)(\phi - x_S)}} + \theta_R\right) \times \left[\frac{b}{\sqrt{\cos^2\phi + \beta_2^2 \sin^2\phi}}\right] \cos\phi \, d\phi \quad (13)$$

$$F_{RT} = F_R + F_A \quad (14)$$

The retention forces were calculated (using the sigmoid fit for contact angle distribution and dual ellipse base area fit) and compared against the gravitational force required for roll-off. Figure 8a shows the gravitational force using the measured roll-off angle on the x-axis vs the calculated retention forces using a circular base assumption and the third-order polynomial contact angle distribution previously introduced for smooth surfaces by ElSherbini and Jacobi.[24] Figure 8b shows the gravitational force using the measured roll-off angle on the x-axis vs the calculated retention forces using a dual ellipse base area and the sigmoid function contact angle distribution introduced in this work for structured SH surfaces. The gray regions in Figure 8 represent a ±20% band on the predictions. The retention force calculated for SH surfaces using the sigmoid contact angle distribution and dual ellipse base area are closer to the determined gravitational forces, showing that the improved sigmoid function and dual ellipse base area are better representations of the drop behavior for both structured SH and smooth HPo surfaces. Indeed, all of the data points lie within ±20% of the predicted values using the approach described above. In contrast, using the polynomial contact angle distribution and circular base assumption, the scatter in the data is much greater. On average, the force difference (averaged over four drop sizes (10−40 μL) and five surface types ($0.03 \le F_S \le 1.0$)) between the drop weight component along the plane and the calculated retention force using a sigmoid contact angle distribution with dual ellipse base area is approximately 50% smaller than that for the retention force calculated using a circular base with polynomial contact angle distribution.

Notice that force values in Figure 8b are calculated using a dual elliptical base area and sigmoid contact angle distribution. In addition to the advancing/receding contact angle values for a given surface, the value of x_S needs to be known to fully specify the sigmoid distribution for calculating retention force. As x_S may not readily be known without experimentation, we note that the value of x_S varies between 70° and 80° for the conditions studied in this work, including for smooth hydrophobic surfaces. In the absence of measured values for smooth and microstructured hydrophobic surfaces, our data would indicate using an x_S in this range.

https://doi.org/10.1021/acs.langmuir.2c02290
Langmuir 2022, 38, 15960−15972

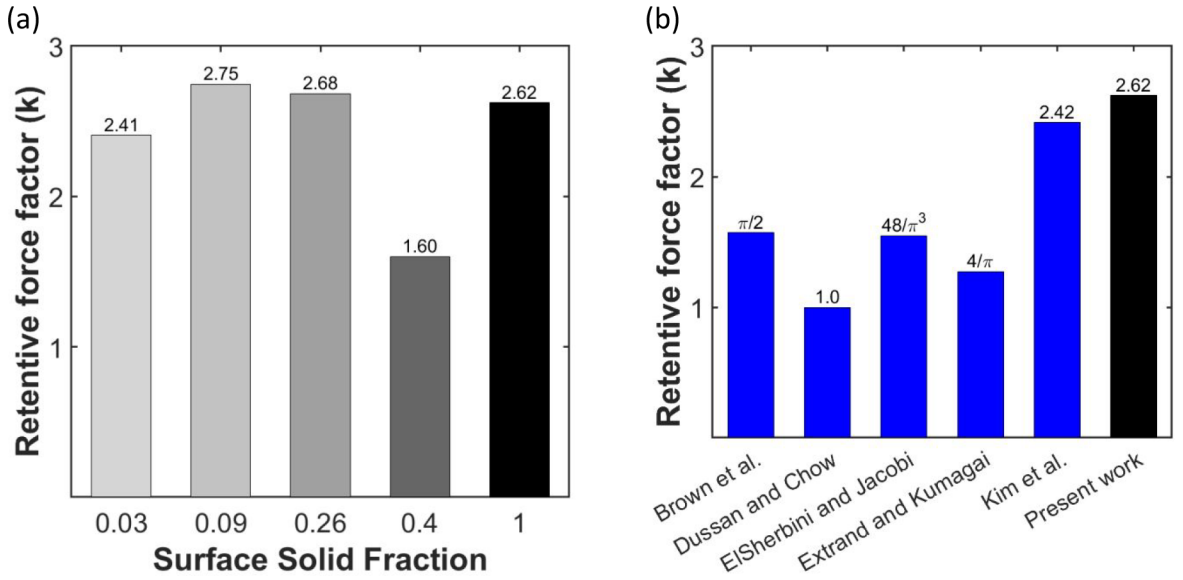

Figure 9. (a) Retentive force factor k for different surface solid fractions averaged over all drop volumes. (b) Comparison of k as reported in the literature for smooth surfaces to present work.[10,11,23,26,33]

Retentive Force Factor. The retentive force factor, k, is calculated in a manner following[23]

$$F_{RT} = k\sigma R_{base}(\cos\theta_R - \cos\theta_A) \quad (15)$$

where k is the retentive force factor and R_{base} is the radius of an equivalent spherical drop of given volume at the solid−liquid interface. R_{base} can be calculated by the equation[31]

$$R_{base} = \left[\frac{3\forall}{\pi}\frac{\sin^3\theta}{(2 - 3\cos\theta + \cos^3\theta)}\right]^{1/3} \quad (16)$$

where $\forall$ is the drop volume and θ is the static contact angle. For this work, the retention force (F_{RT}) in eq 15 is calculated using the sigmoid contact angle distribution and dual ellipse base area described previously. Advancing and receding contact angles are experimentally measured, and R_{base} is calculated for a known drop volume using the equation for the volume of a spherical drop. Results for k are presented in Figure 9, with an uncertainty of ±0.3.

Variation in k with drop volume for each of the surface solid fractions explored in this work (see the Supporting Information). For the uncertainty band of ±0.3, k can be assumed to be independent of drop volume over the range considered, and this was also observed by Kim et al. for drop adhesion energy on smooth surfaces.[33] Average values of k overall drop volumes but at different solid fraction are presented in Figure 9a. As no previous data exist for k on microstructured SH surfaces, Figure 9b provides a comparison of k from the present work with previous studies for smooth HPo surfaces only. Previously, Kim et al.[33] showed that the most commonly used value for k proposed by ElSherbini and Jacobi[11] was not well suited for DI water on any hydrophobic surface coatings. Because the factor k depends on the contact angle distribution and drop shape, use of the third-order polynomial contact angle distribution and spherical drop assumption is expected to be the cause for the discrepancy in the experimental results of Kim et al. and that reported by ElSherbini and Jacobi. For smooth HPo surfaces, our estimation for k of 2.62 using the proposed sigmoid contact angle distribution and dual ellipse base area shape agrees well with the value of Kim et al. (k = 2.42), within the uncertainty of the measurement (see Figure 9b).

Figure 9a shows that the constant k assumption for microstructured SH and smooth HPo surfaces is within the uncertainty range, except at F_S = 0.4. As previously observed, elongation and contact angle hysteresis variation is higher toward larger solid fraction surfaces (for F_S from 0.26 to 1) where the data resolution is low. Therefore, it is not clear whether or not k is constant for the entire solid fraction range. In addition, as the minimum-energy state for drops on microstructured SH surface depends on the microstructure pitch, diameter, and height, the exact state of the drop resting on a microstructured SH surface is somewhat unclear.[31] As previously stated, drops are claimed to be in the Cassie−Baxter or partial wetted state based on experimental evidence for the drop volume range used in the present work. The retention force for a Cassie drop resting on microstructured post surface without any overhanging liquid volume will be different from the adhesion force of a partially wetted drop resting on a microstructured post surface with the overhanging part between the posts. For this reason, using a retentive force factor like k to generalize and predict retentive force for drops on microstructured SH is not recommended.

CONCLUSIONS

Retention forces for drops on micropillar structured SH surfaces with various solid fractions were examined under the influence of gravity. Roll-off angles for each drop volume were measured on various solid fraction surfaces. The circumferentially varying contact angle distribution along the three-phase contact line and the base area of the drop were determined experimentally. These two parameters were used to calculate the retention force between the drop and the surface.

A sigmoid function was shown to provide an improved fit for the drop contact angle distribution on micropillar structured SH surfaces compared to previously suggested distributions. Parameters used in the sigmoid function are physically relevant and are based on the advancing and receding contact angles. In

https://doi.org/10.1021/acs.langmuir.2c02290
Langmuir 2022, 38, 15960−15972

addition, the sigmoid function reduces close to a symmetric curve ($x_S \cong 80°$) that is valid for smooth hydrophobic surfaces ($F_S = 1$), resulting in better retention force estimates. On the basis of the data obtained for the smooth HPo and structured SH surfaces in this work, advancing and receding contact angles were correlated as a function solid fraction. The functions can be used to predict the contact angle distribution for any given solid fraction of the surface with comparable features sizes as explored in this study.

The drop base area for a micropillar, structured SH surface can be best represented with a combination of two ellipses. The receding side of the drop's base elongates more than the advancing side and therefore has a different axis ratio than the advancing side. The advancing side of the drop base area is observed to be generally circular with only slight elongations for intermediate solid fraction surfaces ($F_S = 0.26, 0.4$) The base area of a smooth hydrophobic surface is circular overall, resulting in β_1 and β_2 values that approach unity.

When the suggested base area and sigmoid function for contact angle distribution are used to calculate retention forces, the predicted results are better than previously proposed models of contact angle distribution and base area shape. Overall, retention forces calculated with the sigmoid contact angle distribution and dual elliptical base area are on average 50% closer to the drop weight than using earlier proposed distributions. With an improved retention force characterization, the forces required to move drops along a structured SH surface can be determined more accurately, and this has implications where dropwise condensation prevails.

Retention forces for smooth and microstructured SH surfaces calculated using sigmoid contact angle distribution and dual ellipse base area were used to suggest retention force factor values for varying solid fraction surfaces. The current work indicates a higher value of k for smooth HPo surfaces than several previous studies. However, base area and contact angle hysteresis trends suggest that using a retention force factor to prediction retention forces may not be appropriate, especially for higher solid fractions. Rather, this work indicates using a dual ellipse base area and sigmoid contact angle relation to calculate retention forces is preferable for drops on microstructured SH surfaces.

■ ASSOCIATED CONTENT

Supporting Information

The Supporting Information is available free of charge at https://pubs.acs.org/doi/10.1021/acs.langmuir.2c02290.

SEM image of typical surface, additional retentive force factor data, and contact angle distribution for varying drop volume (PDF)

■ AUTHOR INFORMATION

Corresponding Author

Brian D. Iverson − *Brigham Young University, Provo, Utah 84602, United States;* orcid.org/0000-0002-4592-3728; Email: bdiverson@byu.edu

Authors

Shaur Humayun − *Brigham Young University, Provo, Utah 84602, United States*

R. Daniel Maynes − *Brigham Young University, Provo, Utah 84602, United States*

Julie Crockett − *Brigham Young University, Provo, Utah 84602, United States*

Complete contact information is available at: https://pubs.acs.org/10.1021/acs.langmuir.2c02290

Notes

The authors declare no competing financial interest.

■ ACKNOWLEDGMENTS

This material is based upon work supported by the National Science Foundation under Grant No. 1805805.

■ NOMENCLATURE

D, diameter of capillary tube (m)
DWC, dropwise condensation
F_A, advancing retention force (μN)
F_R, receding retention force (μN)
F_{RT}, retention force (μN)
F_S, solid fraction
g, gravitational constant (m/s^2)
h, rise of water in capillary tube (m)
HPo, hydrophobic
k, retentive force factor
m, mass of drop (kg)
r, radial distance from center of drop to three phase contact line (m)
R_{base}, base radius (m)
SH, superhydrophobic
x_S, shift along x-axis (deg)
$\forall$, drop volume (m^3)

Greek Letters

α, roll-off angle (deg)
β_1, receding ellipse axis ratio
β_2, advancing ellipse axis ratio
θ, contact angle (deg)
θ_A, advancing contact angle (deg)
θ_{app}, apparent contact angle (deg)
θ_I, intrinsic contact angle (deg)
θ_R, receding contact angle (deg)
ρ, density (kg/m^3)
σ, surface tension (N/m)
ϕ, azimuthal position (deg)
ϕ', corrected azimuthal position (deg)

■ REFERENCES

(1) Stevens, K. A.; Crockett, J.; Maynes, D. R.; Iverson, B. D. Two-phase flow pressure drop in superhydrophobic channels. *Int. J. Heat Mass Transfer* **2017**, *110*, 515−522.

(2) Stevens, K. A.; Crockett, J.; Maynes, D.; Iverson, B. D. Simulation of Drop-Size Distribution During Dropwise and Jumping Drop Condensation on a Vertical Surface: Implications for Heat Transfer Modeling. *Langmuir* **2019**, *35*, 12858.

(3) Ma, M.; Hill, R. M. Superhydrophobic surfaces. *Curr. Opin. Colloid Interface Sci.* **2006**, *11* (4), 193−202.

(4) Sheng, C.; Yang, L.; Zhang, H.; Zhang, P.; Shen, G. One-step hydrothermal method to prepare superhydrophobic cotton fabric with antibacterial properties. *J. Eng. Fiber. Fabr.* **2021**, *16*, 155892502110660.

(5) Wu, Z.; Sun, H.; Xu, Z.; Chi, H.; Li, X.; Wang, S.; Zhang, T.; Zhao, Y. Underwater Mechanically Tough, Elastic, Superhydrophilic Cellulose Nanofiber-Based Aerogels for Water-in-Oil Emulsion Separation and Solar Steam Generation. *ACS Appl. Nano Mater.* **2021**, *4*, 8979−8989.

(6) Chen, X.; Wu, X.; Li, F.; Zhao, X.; Wang, S. Enhancement of Condensation Heat Transfer, Anti-Frosting and Water Harvesting by Hybrid Wettability Coating. *Nano* **2021**, *16* (8), 2150086.
(7) Jiang, Y.; Choi, C. H. Droplet Retention on Superhydrophobic Surfaces: A Critical Review. *Adv. Mater. Interfaces* **2021**, *8*, 2001205.
(8) Rose, J. W. Dropwise condensation theory and experiment: A review. *Proceedings of the Institution of Mechanical Engineers, Part A: Journal of Power and Energy* **2002**, *216* (2), 115−128.
(9) El Fil, B.; Kini, G.; Garimella, S. A review of dropwise condensation: Theory, modeling, experiments, applications. *Int. J. Heat Mass Transfer* **2020**, *160*, 120172.
(10) Brown, R. A.; Orr, F. M.; Scriven, L. E. Static drop on an inclined plate: Analysis by the finite element method. *J. Colloid Interface Sci.* **1980**, *73* (1), 76−87.
(11) ElSherbini, A. I.; Jacobi, A. M. Retention forces and contact angles for critical liquid drops on non-horizontal surfaces. *J. Colloid Interface Sci.* **2006**, *299* (2), 841−849.
(12) Yao, C. W.; Tang, S.; Sebastian, D.; Tadmor, R. Sliding of water droplets on micropillar-structured superhydrophobic surfaces. *Appl. Surf. Sci.* **2020**, *504*, 144493.
(13) Tang, S.; Bhimavarapu, Y.; Gulec, S.; Das, R.; Liu, J.; N'guessan, H.; Whitehead, T.; Yao, C. W.; Tadmor, R. Droplets Sliding down a Vertical Surface under Increasing Horizontal Forces. *Langmuir* **2019**, *35* (25), 8191−8198.
(14) Gao, N.; Geyer, F.; Pilat, D. W.; Wooh, S.; Vollmer, D.; Butt, H. J.; Berger, R. How drops start sliding over solid surfaces. *Nat. Phys.* **2018**, *14* (2), 191−196.
(15) Al-Sharafi, A.; Yilbas, B. S.; Ali, H. Water Droplet Adhesion on Hydrophobic Surfaces: Influence of Droplet Size and Inclination Angle of Surface on Adhesion Force. *J. Fluids Eng. Trans. ASME* **2017**, *139* (8), 081302.
(16) Lee, J. M.; Lee, S. H.; Ko, J. S. Dynamic lateral adhesion force of water droplets on microstructured hydrophobic surfaces. *Sensors Actuators, B Chem.* **2015**, *213*, 360−367.
(17) Farhat, N.; Alen, S. K.; Rahman, M. A. Numerical study of the wetting and mobility of liquid droplets on horizontal and inclined flat and microgrooved surfaces. *6th BSME International Conference on Thermal Engineering (ICTE 2014)* **2015**, *105*, 576−585.
(18) Yoon, Y.; Jo, Y.; Kim, H. S. Experimental investigation of liquid water droplet removal in a simulated polymer electrolyte membrane fuel cell gas channel with gas diffusion layer characteristics. *J. Mech. Sci. Technol.* **2014**, *28* (12), 5221−5230.
(19) Pilat, D. W.; Papadopoulos, P.; Schäffel, D.; Vollmer, D.; Berger, R.; Butt, H. J. Dynamic measurement of the force required to move a liquid drop on a solid surface. *Langmuir* **2012**, *28* (49), 16812−16820.
(20) Sabry, M.-N.; ElGharieb, E. Droplet dynamics over a super hydrophobic surface,. *3rd Int. Conf. Therm. Issues Emerg. Technol. Theory Appl.* **2010**, 137−143.
(21) Furmidge, C. G. L. Studies At Phase Interfaces I. the Sliding of Liquid Drops on Solid Surfaces and a Theory for Spray Retention. *J. Colloid Sci.* **1962**, *17*, 309−324.
(22) Korte, C.; Jacobi, A. M. Condensate retention effects on the performance of plain-fin-and-tube heat exchangers: Retention data and modeling. *J. Heat Transfer* **2001**, *123* (5), 926−936.
(23) Extrand, C.; Kumagai, Y. Liquid Drops on an Inclined Plane: The Relation between Contact Angles, Drop Shape, Retentive Force. *J. Colloid Interface Sci.* **1995**, *170*, 515−521.
(24) ElSherbini, A. I.; Jacobi, A. M. Liquid drops on vertical and inclined surfaces: I. An experimental study of drop geometry. *J. Colloid Interface Sci.* **2004**, *273* (2), 556−565.
(25) Rotenberg, Y.; Boruvka, L.; Neumann, A. W. The shape of non-axisymmetric bubbles on inclined planar surfaces. *Colloids Surfaces A Physicochem. Eng. Asp.* **1984**, *102* (2), 424−434.
(26) Dussan, E. B.; Chow, V. R. T.-P. On the ability of drops or bubbles to stick to non-horizontal surfaces of solids. *J. Fluid Mech.* **1985**, *151* (1), 1.
(27) Sommers, A. D.; Jacobi, A. M. Wetting phenomena on micro-grooved aluminum surfaces and modeling of the critical droplet size,. *J. Colloid Interface Sci.* **2008**, *328* (2), 402−411.
(28) Antonini, C.; Carmona, F. J.; Pierce, E.; Marengo, M.; Amirfazli, A. General methodology for evaluating the adhesion force of drops and bubbles on solid surfaces. *Langmuir* **2009**, *25* (11), 6143−6154.
(29) Liu, T.; Sun, W.; Sun, X.; Ai, H. Thermodynamic analysis of the effect of the hierarchical architecture of a superhydrophobic surface on a condensed drop state. *Langmuir* **2010**, *26* (18), 14835−14841.
(30) Whyman, G.; Bormashenko, E.; Stein, T. The rigorous derivation of Young, Cassie-Baxter and Wenzel equations and the analysis of the contact angle hysteresis phenomenon. *Chem. Phys. Lett.* **2008**, *450* (4−6), 355−359.
(31) Liu, T.; Sun, W.; Li, X.; Sun, X.; Ai, H. Growth modes of condensates on nano-textured surfaces and mechanism of partially wetted droplet formation. *Soft Matter* **2013**, *9* (41), 9807−9815.
(32) Miwa, M.; Nakajima, A.; Fujishima, A.; Hashimoto, K.; Watanabe, T. Effects of the surface roughness on sliding angles of water droplets on superhydrophobic surfaces. *Langmuir* **2000**, *16* (13), 5754−5760.
(33) Kim, Y. H.; Kim, K.; Jeong, J. H. Determination of the adhesion energy of liquid droplets on a hydrophobic flat surface considering the contact area. *Int. J. Heat Mass Transfer* **2016**, *102*, 826−832.
(34) Xiang, T.; Chen, D.; Lv, Z.; Yang, Z.; Yang, L.; Li, C. Robust superhydrophobic coating with superior corrosion resistance. *J. Alloys Compd.* **2019**, *798*, 320−325.
(35) Extrand, C. W. Origins of Wetting. *Langmuir* **2016**, *32* (31), 7697−7706.
(36) Narhe, R. D.; Beysens, D. A. Growth dynamics of water drops on a square-pattern rough hydrophobic surface. *Langmuir* **2007**, *23* (12), 6486−6489.

https://doi.org/10.1021/acs.langmuir.2c02290
Langmuir 2022, 38, 15960−15972